# *In-Situ* Detection and Analysis of Laser-Induced Damage on a 1.5-m Multilayer-Dielectric Grating Compressor for High-Energy, Petawatt-Class Laser Systems

## Introduction

Understanding the *in-situ* laser-induced–damage threshold of large-aperture multilayer-dielectric-diffraction (MLD) gratings is paramount for petawatt-class laser facilities to reach design energies.[1–8] Until now, short-pulse damage testing has been performed only on small-scale samples.[9–15] No vacuum-damage test data are available on large-scale MLD gratings, and it has not been proven that one can simply transfer the results of the small samples to full-aperture MLD gratings. This article reports on the performance and findings of a vacuum-compatible grating-inspection system (GIS) that was deployed to detect *in-situ* damages of large-aperture gratings between high-energy shots. The deployment of a GIS makes it possible to operate OMEGA EP[1] safely and effectively because the morphological change of the compressor-grating-surface feature can be monitored in real-time without breaking the vacuum. The following sections (1) describe the mechanism and characterization of the inspection system; (2) introduce the methodology for detecting grating damage and the analysis method for determining the laser-beam fluence causing damage growth; (3) discuss the accuracy of the determined laser-beam fluence; (4) compare the damage-test result of a large-aperture MLD grating to the damage-probability measurement conducted on a small-grating witness sample; and (5) present conclusions.

## Grating-Damage Inspection System

The grating-based pulse compressor of the petawatt-class, short-pulse OMEGA EP laser consists of four sets of tiled-grating assemblies, each measuring 141 cm × 43 cm (Refs. 1 and 16). The line density of the gratings is 1740 lines/mm. The incident and diffraction angles of the laser beam on grating 4 are 61.4° and 72.5°, respectively. During a recent 15-ps, 2.2-kJ energy ramp, it was imperative to monitor the damage growth of the final grating (grating 4) between shots to ensure that damage did not grow to a size that would damage downstream optics. A GIS, illustrated in Fig. 121.19(a), was deployed in the compressor vacuum chamber to detect damage growth on grating 4 during the energy ramp.

The GIS consists of a line-shape illumination generator and an imaging system. The optical layout of the line generator is illustrated in Fig. 121.19(b). A point source from a fiber-based, 1053-nm continuous-wave laser is projected to form a line-shape illumination pattern on the surface of grating 4 using a multi-element lens assembly. An aspheric singlet collimates the light from the fiber and is followed by a half-wave plate used to adjust polarization of the illumination beam. Two spherical lenses focus the light onto a grating surface ~2 m away. The lens pair was designed to provide a $1/e^2$ spot width of approximately 1 mm at the grating. A negative cylindrical lens located after
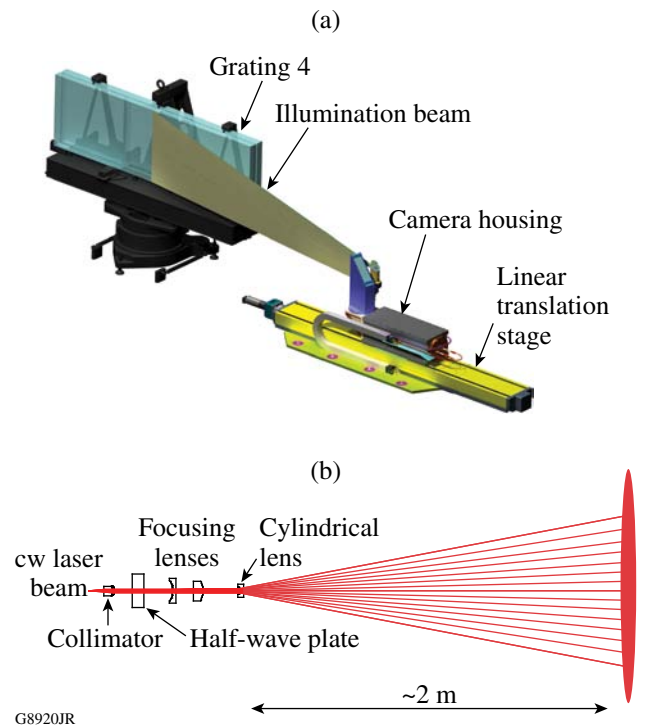


Figure 121.19

(a) The grating-inspection system scans through a $1.5 \times 0.43$-m large-aperture tiled-grating assembly. (b) Optical layout of the line-shape illumination generator of the grating-damage inspection system.

the spherical lens pair spreads the light in a direction parallel to the grating grooves, perpendicular to the scanning direction. The line length and associated illumination falloff along that direction are determined by the focal length of the cylindrical lens. Successive iterations of the design resulted in a trade-off between illumination uniformity and energy loss from light dispersed past the grating edges. The realized illumination pattern is shown in Fig. 121.20. The line length at 50% and the $1/e^2$ intensity are 243 mm and 450 mm, respectively. The angle between the illumination beam and grating normal is 80°. This line-shape illumination is scanned across the grating, and light scattered from any features on the surface is imaged to a 10-bit
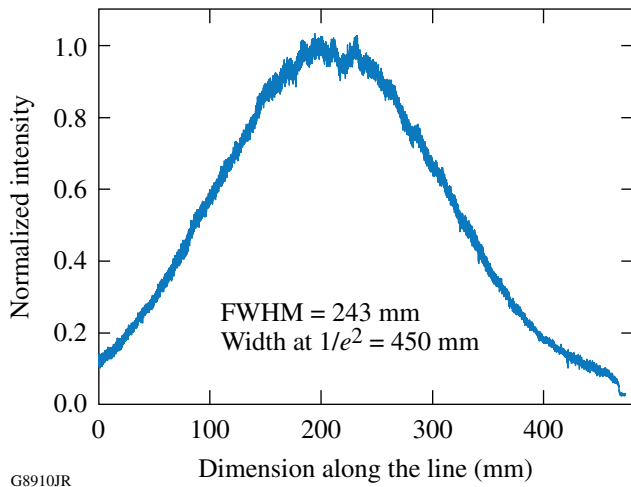
G8910JR

Figure 121.20
Illumination on the surface of grating 4 exhibits a Gaussian pattern along the groove direction.

charge-coupled device (CCD), having $8192 \times 1$ pixels with $7\text{-}\mu\text{m} \times 7\text{-}\mu\text{m}$ pixel size. The CCD is scanned across the grating along with the line-shape generator. The scanned images are then combined to generate a composite two-dimensional (2-D) image of the grating surface. The spatial resolution of a GIS image is limited by the modulation transfer function (MTF) of the imaging system, which was measured to be 0.4 cycle/mm and 1 cycle/mm in horizontal and vertical directions, respectively, at a modulation level of 20%.

***In-Situ* Grating-Damage Detection and Damage Analysis**

Before the energy ramp, a reference scan of grating 4 was taken to record any existing features on the grating surface. An on-shot near-field fluence map was measured for each high-energy shot, and a GIS image was obtained after each shot. Six shots delivered the following energies to grating 4: 1.12 kJ, 1.33 kJ, 1.58 kJ, 1.82 kJ, 1.95 kJ, and 2.20 kJ. The corresponding laser-beam peak fluences were 2.5 J/cm$^2$, 2.7 J/cm$^2$, 3.3 J/cm$^2$, 3.6 J/cm$^2$, 4.0 J/cm$^2$, and 4.6 J/cm$^2$. The nominal pulse width was 15 ps. The near-field imaging system measuring the laser-beam fluence map resides downstream of the grating compressor, as shown in Fig. 121.21(a). During each high-energy shot, 0.7% of the main laser beam was delivered to the short-pulse–diagnostics path (SPDP) through a diagnostic mirror. This sample beam was then down-collimated, further attenuated, and sent to a near-field CCD, imaged to grating 4 for energy and fluence measurement. Figure 121.21(b) shows the scanned image of grating 4 after the 2.2-kJ shot. A majority of the damage features reside in areas ROI 1 and ROI 2 (ROI: region of interest); these two ROI's were chosen for damage analysis. Some of the features on this image were intrinsic to
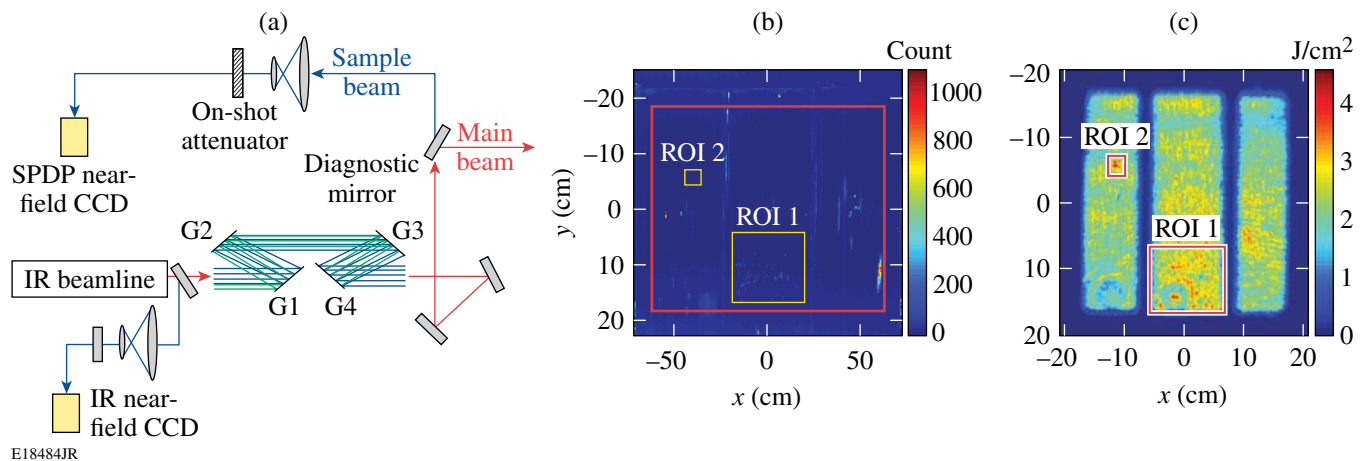
E18484JR

Figure 121.21
(a) The on-shot laser-fluence measurement path in relation to the grating compressor and the main-beam path; (b) a GIS image after the 2.2-kJ laser shot; (c) a beam-fluence map of the 2.2-kJ laser shot.

the holographic patterning of the gratings, and some existed prior to the energy ramp. Figure 121.21(c) shows the corresponding beam fluence measured on the 2.2-kJ shot. The main beam was shadowed along the gaps of the three individual tiles of grating 4. There is a factor of 0.3 scaling reduction in the $x$ direction between Figs. 121.21(b) and 121.21(c). This is due to the 72.5° angle between the diagnostic beam and the normal of grating 4. Comparative analysis of the scanned images before and after each shot was used to assess any damage initiation and growth. By spatially registering the scanned image of the grating surface to the fluence map and by correlating the identified feature size and peak beam fluence within a specified ROI for each subsequent shot, the upper fluence limit below which damage growth occurred can be determined.

A scanned image of grating 4 was taken after each high-energy shot. Features in the image were identified using various image-processing techniques: A raw image was filtered and properly down-sampled based on the MTF limitation of the imaging system of the GIS. For each specified ROI in the image [shown in Fig. 121.21(b)], the corresponding portion of the down-sampled image was binarized for subsequent feature identification. The portion of the image within an ROI having intensity higher than the binarization threshold was identified as a feature. The binarization threshold was determined using the statistical intensity information of the background and the scattering patterns within an ROI. The location and area size of each identified feature were calculated. Although the identified features exhibit various shapes, for ease of comparison between shots, the equivalent diameter of an identified feature was defined as the diameter of a circle that has the same area size as the identified feature. The histogram of the identified features was defined as the number of features at various equivalent diameters. This property was calculated for each ROI after each high-energy shot. The identified features in ROI 1 prior to the energy ramp are illustrated in Fig. 121.22(a). (Note that
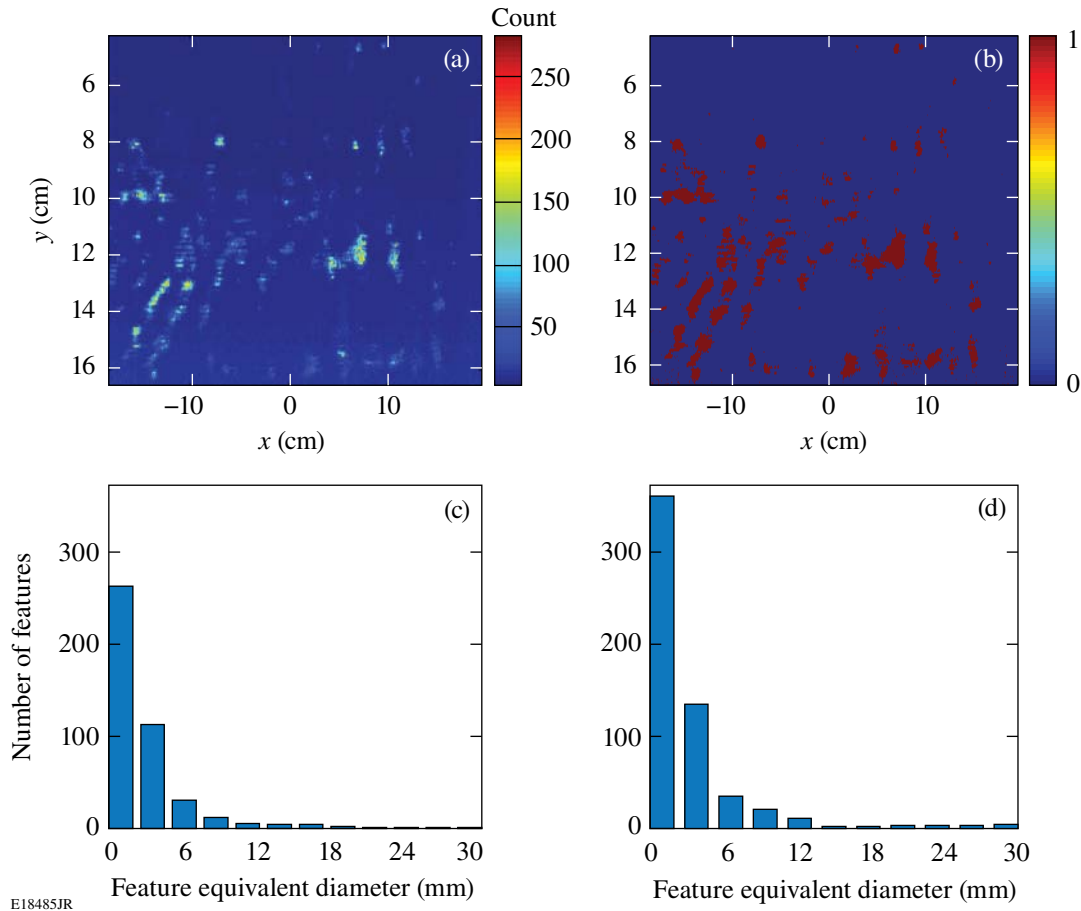


Figure 121.22
(a) Detected features in ROI 1 prior to the energy ramp; (b) binarized image of the detected features in ROI 1 prior to the energy ramp; (c) histogram of the detected features after the 1120-J shot; (d) histogram of the detected features after the 2210-J shot.

there are already a significant number of features in this ROI.) Figure 121.22(b) shows the corresponding binarized image of Fig. 121.22(a). Figures 121.22(c) and 121.22(d) illustrate the histograms of the detected features within ROI 1 prior to and after the energy ramp, respectively. Comparing histograms of damage sites of two consecutive shots, one can determine the shot energy that caused significant amounts of damage growth.

Owing to the fact that it is very challenging to register the grating-damage map and the beam-fluence map within high precision, the peak fluence within a ROI was used to estimate the upper limit of the fluence causing damage growth within that area. ROI 2 [also shown in Fig. 121.21(b)], measuring 23 mm × 24 mm of grating 4, had no GIS-detectable features before the energy ramp and exhibited significant change after the completion of the energy ramp. This region was chosen to determine the upper limit of the incident fluence causing damage initiation and growth. The binarized scanning image, dimensions scaled to the laser-beam space, and the corresponding fluence map within ROI 2 for 2.2-kJ shot energy are shown in Figs. 121.23(a) and 121.23(b). The growth in damage versus peak fluence in ROI 2 is shown in Fig. 121.23(c). The fluence at which significant growth in damage occurred was determined to be 3.3 J/cm$^2$. This fluence was measured normal to the laser beam (72.5° relative to the grating normal). The corresponding shot energy was 1.58 kJ. The signal on the streak camera used for pulse measurement was saturated on this shot; therefore, no valid pulse measurement was obtained. Our on-shot pulse-prediction model predicted a narrowed, 12.9-ps (FWHM intensity) pulse due to dispersion induced by nonlinear phase accumulations in the glass amplifiers.[17] A similar analysis performed for ROI 1 showed a consistent result.

**Accuracy of Peak-Fluence Measurement**

The spatial resolution of the fluence measurement [Fig. 121.21(c)] was limited by the coherent transfer function (CTF) of the imaging system. The CTF cutoff frequency of the near-field imaging system was measured to be 0.25 cycles/mm. In addition, this imaging system is downstream of grating 4; therefore, the measurement of the beam fluence at a given location could have been affected by damage that existed prior to a particular shot. It is worth verifying that the peak-fluence measurement was not distorted by any damage on the optics of the diagnostics chain. To estimate the accuracy of peak flu-ence determined for a given ROI, the image from a different on-shot near-field imaging system was used. This system is located just upstream of the grating compressor [illustrated as IR near-field CCD in Fig. 121.21(a)], and its spatial resolution was measured to be 3× better than the one used to measure
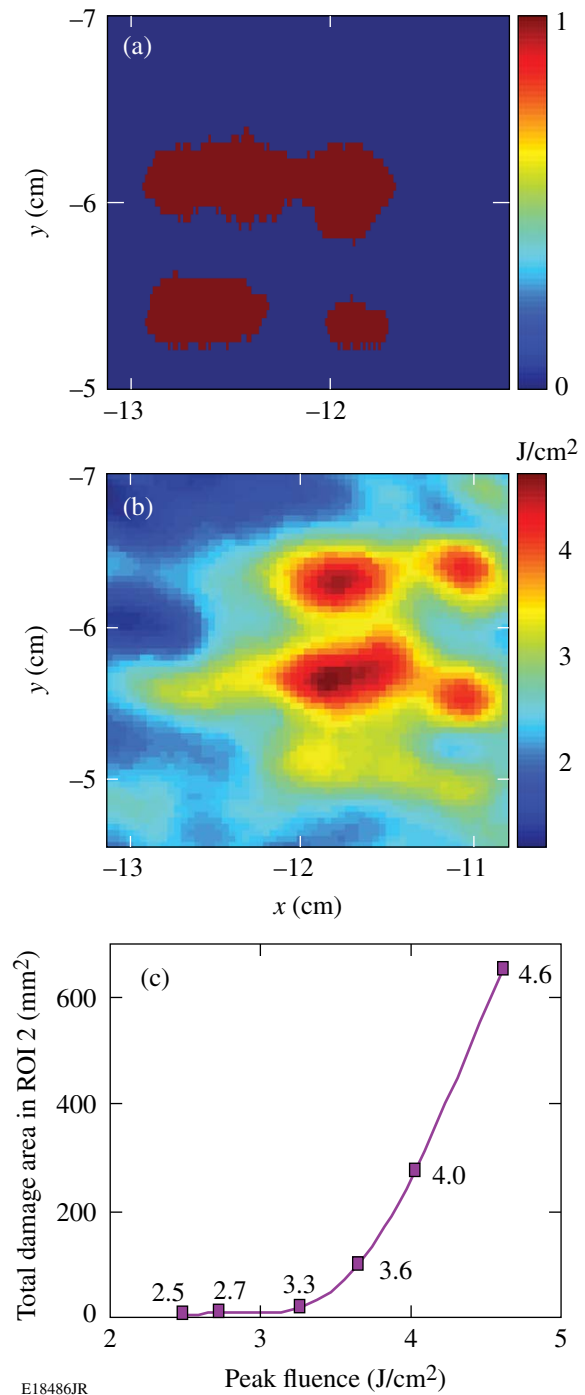


Figure 121.23
(a) Detected features in ROI 2 after the energy ramp; (b) fluence map of ROI 2 of the 2.2-kJ shot; (c) damage size versus beam fluence.

fluence. We then used a propagation model of the compressor, which includes the estimated phase of the beam at the input to the compressor and the phase and intensity effects caused by the compressor, to propagate the fluence map measured at the

input to the compressor to the grating-4 plane. Figure 121.24(a) shows the modeled fluence map for the 2.2-kJ shot. Comparing this fluence map to the measured beam fluence [for ease of comparison, Fig. 121.21(c) is repeated as Fig. 121.24(b)], the measured on-shot peak fluence agrees with the modeled result within 3% and represents the accurate on-shot fluence at grating 4.

## Correlation to the Damage-Test Results Obtained on Small Grating Samples

Damage probability versus beam fluence was measured in vacuum on a small-scale, 100-mm-diam MLD-grating sample. This piece was the fabrication witness sample of the large-scale gratings deployed on OMEGA EP. Figure 121.25(a) shows the layout of the damage-test setup for sample gratings.

An excitation beam with a pulse width of 11.5 ps (FWHM) for inducing damage and a 1053-nm continuous-wave illumination beam for detecting damage were co-aligned and co-focused to a 420-$\mu$m (width at FWHM) focal spot on the grating surface. The incidence angle of the two beams was 61.4° relative to grating normal. The illumination beam was shuttered during the damage excitation process and was turned on afterward for damage detection. The illumination light was scattered by the induced-damage sites and was imaged to a CCD. The resolution of the CCD was 10 $\mu$m/pixel. Change in the scattered image was used to determine the initiation of damage. The sample grating was translated along and across the grating-groove directions for damage tests at various locations. For each fluence, ten sites across the grating sample were chosen, and the percentage of sites damaged was used to determine
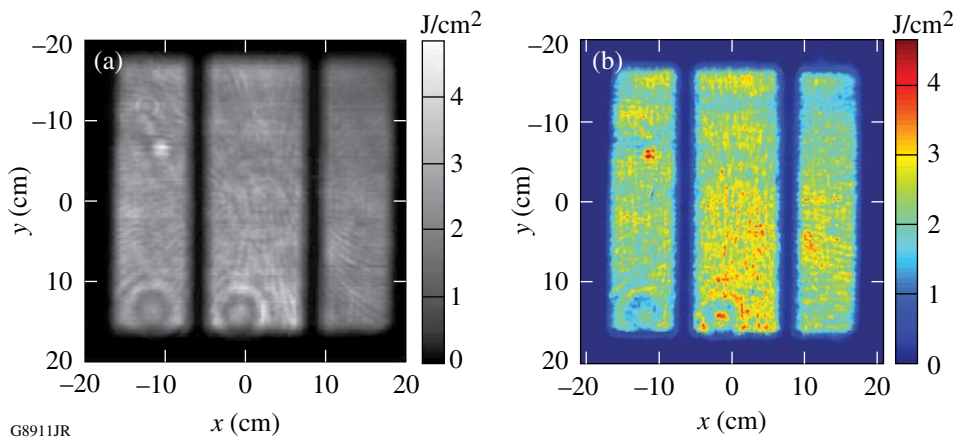


G8911JR

Figure 121.24
(a) The modeled fluence map using the measured fluence at the input of the compressor; (b) measured-beam-fluence map of the 2.2-kJ laser shot.
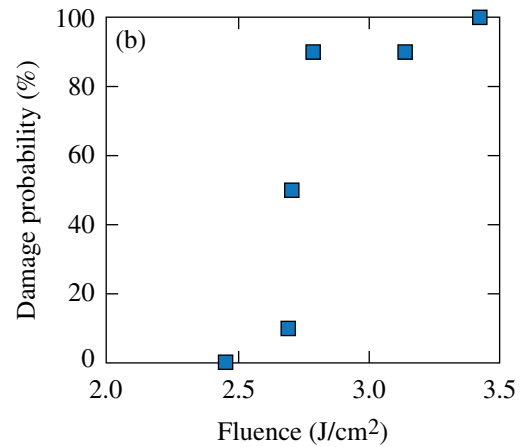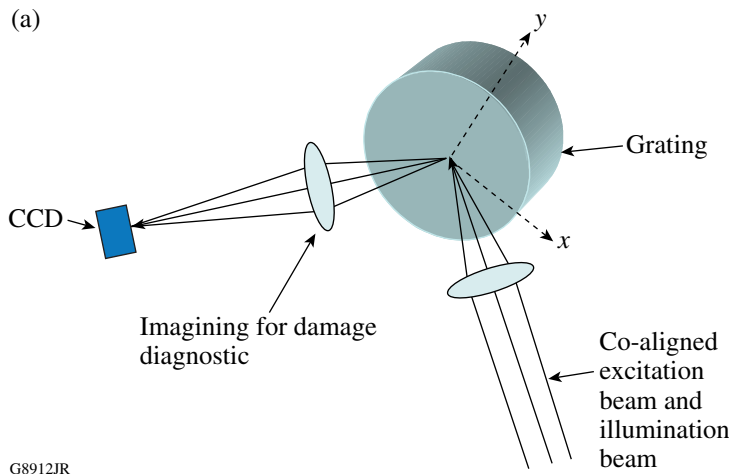


G8912JR

Figure 121.25
(a) Damage-test setup for damage probability at various beam fluences; (b) damage probability versus beam fluence measured on a 100-mm MLD-grating sample in vacuum.

damage probability. Figure 121.25(b) shows damage probability versus peak beam fluence. To compare with damage-test results of the large-aperture grating, the fluence was scaled to the beam space 72.5° relative to grating normal. As shown in Fig. 121.25(b), all ten sites under test were damaged at a fluence of 3.4 J/cm$^2$. This result is consistent with the determined fluence, where significant growth in damage occurred for a 12.9-ps pulse on large-scale gratings, taking into account that damage threshold scales approximately with the square root of the pulse length.[18] This is the first damage test comparison between a small-sized witness sample and a large-scale grating. More tests will be conducted and results will be reported in a subsequent publication.

## Conclusions

A vacuum-compatible grating-inspection system has been developed to measure the *in-situ* laser-induced damage of a 1.5-m tiled-grating assembly of the OMEGA EP pulse compressor during a 15-ps, 2.2-kJ energy ramp. The grating surface scanning image after each high-energy shot was correlated to the on-shot laser-beam fluence map to determine the relation between damage growth and beam fluence. The upper limit of the fluence at which significant grating-damage growth occurred was determined to be 3.3 J/cm$^2$. This result is consistent with damage-probability measurement conducted on a 100-mm-diam witness-grating sample: the measured peak fluence at which 100% selected sites on the small sample were damaged was 3.4 J/cm$^2$. The deployment of a GIS makes it possible to operate OMEGA EP safely and effectively because the morphological change of the compressor-grating-surface feature can be monitored in real-time without breaking the vacuum. For future work, the damage-probability measurement on a large-scale grating can be conducted using the damage-detection analysis technique described here. The correlation between grating-damage growth, morphological change, and grating diffraction efficiency degradation should be investigated.

## REFERENCES

1. J. H. Kelly, L. J. Waxer, V. Bagnoud, I. A. Begishev, J. Bromage, B. E. Kruschwitz, T. J. Kessler, S. J. Loucks, D. N. Maywar, R. L. McCrory, D. D. Meyerhofer, S. F. B. Morse, J. B. Oliver, A. L. Rigatti, A. W. Schmid, C. Stoeckl, S. Dalton, L. Folnsbee, M. J. Guardalben, R. Jungquist, J. Puth, M. J. Shoup III, D. Weiner, and J. D. Zuegel, J. Phys. IV France **133**, 75 (2006).

2. C. P. J. Barty *et al.*, Nucl. Fusion **44**, S266 (2004).

3. N. Blanchot *et al.*, in *Topical Problems of Nonlinear Wave Physics*, edited by A. M. Sergeev (SPIE, Bellingham, WA, 2006), Vol. 5975, p. 59750C.

4. C. Le Blanc *et al.*, in *Inertial Fusion Sciences and Applications 2003*, edited by B. A. Hammel, D. D. Meyerhofer, J. Meyer-ter-Vehn, and H. Azechi (American Nuclear Society, La Grange Park, IL, 2004), pp. 608–611.

5. C. N. Danson *et al.*, Nucl. Fusion **44**, S239 (2004).

6. K. Mima *et al.*, Fusion Sci. Technol. **47**, 662 (2005).

7. V. Yanovsky *et al.*, Opt. Express **16**, 2109 (2008).

8. M. Martinez *et al.*, in *Laser-Induced Damage in Optical Materials: 2005*, edited by G. J. Exarhos *et al.* (SPIE, Bellingham, WA, 2006), Vol. 5991, p. 59911N.

9. J. A. Britten *et al.*, in *Laser-Induced Damage in Optical Materials: 2003*, edited by G. J. Exarhos *et al.* (SPIE, Bellingham, WA, 2004), Vol. 5273, pp. 1–7.

10. J. A. Britten *et al.*, in *Laser-Induced Damage in Optical Materials: 1995*, edited by H. E. Bennett *et al.* (SPIE, Bellingham, WA, 1996), Vol. 2714, pp. 511–520.

11. A. Reichart *et al.*, in *Laser-Induced Damage in Optical Materials: 2000*, edited by G. J. Exarhos *et al.* (SPIE, Bellingham, WA, 2001), Vol. 4347, pp. 521–527.

12. F. Canova *et al.*, Opt. Express **15**, 15324 (2007).

13. W.-J. Kong *et al.*, Chin. Opt. Lett. **3**, 181 (2005).

14. A. Cotel *et al.*, presented at the Conference on Lasers and Electro-Optics (CLEO 2005), Baltimore, MD, 22–27 May 2005 (Paper JFB6).

15. J. Neauport *et al.*, Opt. Express **15**, 12508 (2007).

16. J. Qiao, A. Kalb, T. Nguyen, J. Bunkenburg, D. Canning, and J. H. Kelly, Opt. Lett. **33**, 1684 (2008).

17. Y.-H. Chuang, L. Zheng, and D. D. Meyerhofer, IEEE J. Quantum Electron. **29**, 270 (1993).

18. LLE grating-sample test result provided by A. W. Schmid, University of Rochester.